AIAA JOURNAL
Vol. 33, No. 7, July 1995

Model of Transverse Plate Impact Dynamics for Design of Impact Detection Methodologies

J. K. Shaw*
Virginia Polytechnic Institute and State University, Blacksburg, Virginia 24061
J. S. Sirkis†
University of Maryland, College Park, Maryland 20742
E. J. Friebele‡
U.S. Naval Research Laboratory, Washington, D.C. 20375
R. T. Jones§
University of Maryland, College Park, Maryland 20742
and
A. D. Kersey‡
U.S. Naval Research Laboratory, Washington, D.C. 20375

A closed-form analytical description of the deformation in a fully clamped, homogeneous, and isotropic rectangular plate subjected to transverse impact is presented. This solution is developed for use in the design of impact location and magnitude measurement methodologies. The solution is used to design two artificial neural network-based impact location techniques.

I. Introduction

ONE of the targeted technologies in the smart structures area is the health monitoring of structural systems. Of particular interest is the location of low-velocity impacts on structures constructed from plates and shells. Development of impact location techniques, however, is in many cases a time consuming process. Analytical techniques can be used to make impact detection development more economical by assessing the feasibility of techniques prior to experimental implementation. This paper describes a method of modeling the response of a fully clamped homogeneous and isotropic rectangular plate subjected to transverse impact for just such a purpose. This paper focuses on homogeneity, both as a first step in the progression toward laminate composite applications and because of the direct relevance of homogeneous plate structures in spacecraft applications. In the latter case, vehicles in low Earth orbit are subject to space debris impact, which in some cases can be sufficiently energetic to cause perforation.[1]

Roughly speaking there are two overall approaches one can take in the impact location and damage detection problems for structures.[2] One can apply either direct remote sensing, such as with acoustic wave techniques, or indirect analytical methods, in which an assessment of location or damage is the output of a model whose inputs are generated by sensor readings. As an example of the direct approach, Gunther et al.[3] used the differential signal arrival times from four sensors mounted on a plate with good success to triangulate in the location of an impact point to centimeter range accuracy. In Kudva et al.,[2] on the other hand, both location and damage (circular hole size in this case) could be inferred from strain readings of multiple sensors. It was pointed out by Kudva et al.[2] that the relationship of inputs and outputs were of such complexity that the use of a neural network was considered appropriate; indeed, Kudva et al.[2] and Elkordy et al.[4] reported on the application of such a network which was trained on the basis of an analytical model implemented through finite element analysis. The present paper takes the latter, analytical approach and, to this extent, is similar in philosophy to research presented by Kudva et al.[2] and Elkordy et al.[4]

The suitability of neural networks arises, as mentioned, precisely when input–output relationships appear in complex patterns; the underlying dynamics of which are either impractically complicated or unavailable.[5,6] Some recent applications of neural nets have included damage detection to bridge elements,[7] vibration control,[8] and identification of chemical species.[9]

The plate dynamics model developed in this paper is used to design a neural network to determine the location of an impact on a clamped metal plate on the basis of strain readings from sensors. The purpose of this study is to determine the feasibility of neural network-based impact location approaches, to establish an architecture type for the network, to estimate ranges of parameters used on its training, and to perform these functions without experiments. An impact location technique that proves successful using the analytical data then warrants application with experiments. Analytical models are used for this evaluation simply because evaluating neural network-based impact detection methodologies requires a large number of parametric studies. Finite element or boundary element methods are less suited for these types of analyses. Toward the purpose of evaluating impact detection approaches, all data used for training are generated from an analytical model, analogous to Kudva et al.[2] and Elkordy et al.,[4] for the time-varying strain produced by simulated impacts. Values for the average strain are derived from an expression for the time-varying displacement of an arbitrary point on the plate. Some of the input data used for training the neural network takes the form of the Fourier transform of integrated strain at several sensor locations, the transform being evaluated at a set of the natural frequencies of the plate. It is convenient to sample the transform at the plate natural frequencies, since it is expected that signal amplitudes will be highest there. One of the questions addressed in this paper concerns the number of modes needed to train a network. To the same extent it must be understood how many impact points (and at what resolution) are necessary to train the network. Answering these questions constitutes settling the overriding issue of whether the whole approach is feasible.

A number of references take up the general question of models for plate and shell displacement,[10–12] but there appears to be no suitably

Received Aug. 11, 1994; revision received Jan. 26, 1995; accepted for publication Jan. 30, 1995. This paper is declared a work of the U.S. Government and is not subject to copyright protection in the United States.

*Professor of Mathematics, Department of Mathematics.
†Director, Center for Smart Structures Research and Development, Department of Mechanical Engineering.
‡Supervisory Research Physicist, Optical Sciences Division.
§Graduate Research Assistant, Department of Mechanical Engineering.

comprehensive mathematical representation of the fully clamped plate which includes damping and relies on the natural frequencies of the plate. Consequently, such a model is developed in Sec. II of this paper. In connection with the general problem of plate and shell impacts, the reader is referred to Yang,[13] Ewins,[14] and Schienberg et al.[15] The compendium provided by Wu et al.[16] contains information and additional references on the subject of training neural networks by analytical simulation of damage states.

The plated dynamics are modeled using Laplace transforms in conjunction with a normal mode expansion technique that uses the solutions for the natural frequencies and mode shapes[17] as basis functions in a series expansion. For simplicity, the forces local to the impact site are assumed to be governed by Hertzian contact even though the plate is not an infinite half-space. The temporal contact is given a sharply decreasing exponential form approximating an impulse function and chosen so that the solution is available essentially in closed form. The time dependence of the solution is handled by Laplace transforming the governing differential equations, after which the spatial dependence is solved using the series approach in the transform domain, and then the inverse is transformed.

II. Analytical Model of Transverse Plate Impact

The results of this paper apply to any isotropic, homogeneous, fully clamped plate of uniform thickness that obeys, in standard coordinates, the governing equation

$$D\Delta^4 w + c\frac{\partial w}{\partial t} + \rho h\frac{\partial^2 w}{\partial t^2} = p(x, y, t) \tag{1}$$

where $0 \le x \le a$ and $0 \le y \le b$ are standard Cartesian coordinates, a and b are the width and height of the plate, $w = w(x, y, t)$ is the transverse displacement, D is the bending stiffness,[17] Δ is the biharmonic operator, ρ is the density of plate material, h is its thickness, c is the damping constant,[14] and $p(x, y, t)$ is the driving function. Specific assumptions about $p(x, y, t)$ are given presently; the form of $p(x, y, t)$, coupled with the solution $u(x, y, t)$, is supposed to stimulate the response of the plate to a low-velocity, nondamaging strike.

A. Eigenfunction Expansion

It is convenient to express the solution of Eq. (1) as an expansion in terms of the natural modes of the plate. For the fully clamped plate, the eigenfunctions $w_l(x, y)$ and eigenvalues τ_l $(l = 1, 2, 3, \ldots)$ are rather complicated but can be calculated to close accuracy. In the analysis of Ref. 17 the mode shapes $w_l(x, y)$ have, for certain constants $A_{mn}^{(l)}$, the form

$$w_l(x, y) = \sum_{m=1}^{\infty}\sum_{n=1}^{\infty} A_{mn}^{(l)} X_m(x) Y_n(y) \tag{2}$$

where the $X_m(x)$ and $Y_n(y)$ are eigenfunctions for a clamped beam problem on $0 \le x \le a$ and $0 \le y \le b$, respectively. Specifically, $X_m(x) = C_m\phi_m(\epsilon_m x/a)$ and $Y_n(y) = D_n\phi_n(\epsilon_n y/b)$, where

$$\phi_k(z) = \cosh(z) - \cos(z) - \alpha_k[\sinh(z) - \sin(z)] \tag{3}$$

where the $\{\epsilon_k\}$ and $\{\alpha_k\}$ sequences are determined as the roots of

$$\cosh\epsilon\cos\epsilon = 1 \qquad \text{and} \qquad \alpha = \frac{[\cosh(\epsilon) - \cos(\epsilon)]}{[\sinh(\epsilon) - \sin(\epsilon)]} \tag{4}$$

and where the constants C_m and D_n are chosen so that

$$\int_0^a X_m^2(x)\,dx = a, \qquad \int_0^a Y_n^2(y)\,dy = b \tag{5}$$

It can be shown that the normalizing constants satisfy

$$C_k = D_k = |\cos(\epsilon_k) - \alpha_k\sin(\epsilon_k)| \tag{6}$$

for $k = 1, 2, 3, \ldots$.

It is easy to calculate the ϵ_k and α_k terms numerically from Eq. (4); the first three terms of the sequences are $\alpha_1 = 0.98250222$, $\alpha_2 = 1.00077731$, $\alpha_3 = 0.99996645$, $\epsilon_1 = 1.7300408$, $\epsilon_2 = 7.8532046$, $\epsilon_3 = 10.9956078$ (Ref. 17). Examining the behavior of $\cosh(\epsilon)\cos(\epsilon)$, it becomes clear that $\alpha_k \sim (2k + 1)\pi/2$, $\epsilon_k \sim 1$, and $C_k = D_k \sim 1$ as $k \to \infty$. The coefficients $A_{mn}^{(l)}$ in Eq. (2) are best thought of as eigenvalues of a characteristic matrix for the plate. The essential form of the matrix will be given here for completeness; more details are provided in the Appendix. Let τ_l be an eigenvalue for the undamped biharmonic operator, under clamped boundary conditions, i.e.,

$$\Delta^4 w_l = \frac{\partial^4 w_l}{\partial x^4} + \frac{\partial^4 w_l}{\partial x^2\partial y^2} + \frac{\partial^4 w_l}{\partial y^4} = \tau_l w_l \tag{7}$$

There is a doubly indexed matrix C_{mn}^{ik}, whose definition is given in Eq. (A1), such that if λ_l is defined by $\lambda_l = \tau_l a^3 b$ $(l = 1, 2, 3, \ldots)$ and if

$$\delta_{mn}^{ik} = \begin{cases} 1, & (m, n) = (i, k) \\ 0, & (m, n) \ne (i, k) \end{cases} \tag{8}$$

then the parameters are all linked by

$$\sum_{m=1}^{\infty}\sum_{n=1}^{\infty}\left(C_{mn}^{ik} - \lambda_l\delta_{mn}^{ik}\right)A_{mn}^{(l)} = 0 \tag{9}$$

where $i, k = 1, 2, 3, \ldots$. Thus, Eq. (9) is an infinite linear system and the $\lambda_1, \lambda_2, \lambda_3, \ldots$ are values of λ_l such that Eq. (9) has a nontrivial solution $\{A_{11}^{(l)}, A_{12}^{(l)}, A_{21}^{(l)}, A_{22}^{(l)}, \ldots\}$; see Ref. 17 and the Appendix for details and an example. Equation (9) is the characteristic equation for the natural plate modes without damping. The method for solving Eq. (1), subject to damping, will be given presently. In Eq. (9) the infinite series is obviously truncated to a finite range; for the calculations presented in the next section, the index range in Eq. (9) is $1 \le m, n \le 4$, $1 \le l \le 16$. It is usually convenient to normalize the coefficients in Eq. (9) by requiring

$$\sum_{m=1}^{\infty}\sum_{n=1}^{\infty}\left(A_{mn}^{(l)}\right)^2 = 1 \tag{10}$$

Having calculated the λ_l and $A_{mn}^{(l)}$ from Eq. (9), one then has the mode shapes $w_l(x, y)$ as in Eq. (2).

B. Solution Method

The most direct way to solve Eq. (1) is by the Laplace transform method. For this purpose it is convenient to assume that $p(x, y, t)$ has separated variables,

$$p(x, y, t) = p_0(t)p_1(x)p_2(y) \tag{11}$$

Letting $P_0(s) = \boldsymbol{L}[p_0(t)](s)$ and $w(x, y, s) = \boldsymbol{L}[w(x, y, t)](s)$ be the transforms of p_0 and u, the transform of Eq. (1) is given by

$$D\Delta^4 w + csw + \rho hs^2 w = p_1(x)p_2(y)P_0(s) \tag{12}$$

where s is the Laplace frequency, and $w(x, y, 0) = w_t(x, y, 0) = 0$ has been assumed. To solve Eq. (1) the right side of Eq. (12) will be expanded in a series of eigenfunctions $w_l(x, y)$. The series for $U(x, y, s)$ will then be found, essentially by the method of undetermined coefficients, and then $u(x, y, t)$ will be obtained by inverse transform. Thus, assume the expansions

$$p_1(x)p_2(y) = \sum_{l=1}^{\infty} b_l w_l(x, y) \tag{13}$$

and

$$W(x, y, s) = \sum_{l=1}^{\infty} B_l(s)w_l(x, y) \tag{14}$$

and substitute into Eq. (12). From $\Delta^4 w_l = \tau_l w_l$ [Eq. (7)] one has

$$\sum_{l=1}^{\infty} B_l(s)\left[D\tau_l + cs + \rho hs^2\right]w_l(x, y) = P_0(s)\sum_{l=1}^{\infty} b_l w_l(x, y) \tag{15}$$

Equating coefficients gives

$$B_l(s) = \frac{b_l P_0(s)/\rho h}{s^2 + (cs/\rho h) + (D\tau_l/\rho h)} \tag{16}$$

which becomes, after introducing $\tilde{a} = (c/\rho h)$ and $\tilde{b}_l = (D\tau_l/\rho h)$,

$$B_l(s) = \frac{b_l P_0(s)/\rho h}{s^2 + \tilde{a}s + \tilde{b}_l} = \frac{b_l P_0(s)/\rho h}{(s + (\tilde{a}/2))^2 + \tilde{B}_l^2}, \tag{17}$$

where $\tilde{B}_l = (\tilde{b}_l - \tilde{a}^2/4)^{1/2}$. The notation in Eq. (17) anticipates taking the inverse transform of Eq. (17) and reveals $(\tilde{a}/2)$ and $\tilde{B}_l$ to be the damping and natural frequency terms, respectively, for the plate. Substituting the inverse transform of Eq. (17) into the inverse transform of Eq. (14) yields

$$w(x, y, t) = \sum_{l=1}^{\infty} \frac{b_l}{\rho h} L^{-1}\left(\frac{P_0(s)}{s^2 + \tilde{a}s + \tilde{b}_l}\right)(t) w_l(x, y) \tag{18}$$

which is the plate response to the forcing function $P(x, y, t) = p_0(t)p_1(x)p_2(y)$. The solution given by Eq. (18) is the basic form used in this paper. The explicit forms of p_0, p_1, and p_2 will now be discussed, beginning with the time dependence $p_0(t)$.

C. Time Dependence

In selecting a form for $p_0(t)$ the goal is to find a functional form that has a simple Laplace transform, if possible, and which represents a physical impact in a realistic way. The time dependence of a strike event should emulate an impulse function but be physically reasonable. Exponential functions have simple transforms and can be tailored to exhibit the steep rise and fall associated with an impact. These remarks suggest the choice

$$p_0(t) = K_0 e^{-M|t - t_0|} \tag{19}$$

where $M \gg 1$, $K_0 \gg 1$, and $t_0 > 0$ represents instant of impact initiation. Expression (19) represents a forcing term concentrated at t_0, of duration inversely proportional to M, and magnitude K_0. The transform of Eq. (19) is

$$P_0(s) = K_0\left(\frac{e^{-st_0}}{M + s} + \frac{e^{-st_0} - e^{-Mt_0}}{M - s}\right) \tag{20}$$

Now the inverse transform of $P_0(s)/(s^2 + \tilde{a}_s + \tilde{b}_l)$ in Eq. (18) must be computed, and for $t > 0$ is

$$L^1\left(\frac{P_0(s)}{(s^2 + \tilde{a}s + \tilde{b}_\ell)}\right)(t) = \frac{2K_0 H(t - t_0) e^{-\tilde{a}(t - t_0)/2}}{(M^2 + \tilde{a}M + \tilde{b}_l)(M^2 - \tilde{a}M + \tilde{b}_l)}$$
$$\times \left\{\frac{(M^2 + b_l)\sin[\tilde{B}_l(t - t_0)]}{\tilde{B}_l} - \tilde{a}M\cos[\tilde{B}_l(t - t_0)]\right\}$$
$$+ R(t, t_0, l) \tag{21}$$

where $H(t)$ is the heavyside step function [$H(t) = 0$ for $t < 0$ and $H(t) = 1$ for $t > 0$] and where $R(t, t_0, l)$ is given in the Appendix [see Eq. (A4)]. The function $R(t, t_0, l)$ contains essentially subdominant terms, which, in the interest of simplicity, is not presented in Eq. (21). One sees in Eq. (21) that $\tilde{a} = c/2\rho h$ is the damping term whereas $\tilde{B}_l$, defined by Eq. (17) and given additionally by

$$\tilde{B}_l^2 = \frac{D\tau_l}{\rho h} - \frac{c^2}{4\rho^2 h^2} = \frac{1}{4\rho^2 h^2}(4D\tau_l \rho h - c^2) \tag{22}$$

is the lth natural frequency of the damped plate.[18] In order that $\tilde{B}_l$ be real valued it is necessary that $c < (4D\tau_l \rho h)^{1/2}$, which constitutes a physical limitation on the damping constant c.

Although Eq. (21) may appear to be complicated, it can be evaluated very quickly by computer since all its elements are built-in functions. In fact, it allows, one to quickly generate a graph of the plate response with very small time steps and a large time range.

D. Spatial Dependence

In Eq. (18) there remains only the term b_l to discuss. By Eq. (13), b_l depends solely on the $p_1(x)p_2(y)$ terms and thus constitutes the spatial dependence of the forcing term. In this analysis the spatial dependence will take the form of uniform pressure exerted over a small rectangular area. Specifically it will be assumed that

$$p_1(x) = K_a\begin{cases} 1, & |x - x_0| < a_0 \\ 0, & \text{otherwise} \end{cases}$$
$$p_2(y) = K_b\begin{cases} 1, & |y - y_0| < b_0 \\ 0, & \text{otherwise} \end{cases} \tag{23}$$

where K_a and K_b are magnitude constants and (x_0, y_0) is the center of the impact area consisting of the rectangle $x_0 - a_0 \le x \le x_0 + a_0$, $y_0 - a_0 \le x \le y_0 + a_0$. The form of Eq. (23) is advantageous in that the coefficients b_l can be calculated in relatively simple closed form. In Eq. (23), (x_0, y_0) will range over the plate whereas a_0 and b_0 will be kept small. Assuming a rectangular impact area should not be a source of concern in modeling global plate response, because by the St. Venant's principle the specific local strain patterns have little effect on the overall displacement at points (x, y) sufficiently far removed from (x_0, y_0). On a multisensory plate one is assured that the majority of sensors will be remote from the impact point. The explicit form of b_l under assumption in Eq. (23) can be calculated to be

$$b_l = (ab)^{-1}\sum_{m=1}^{\infty}\sum_{n=1}^{\infty} A_{mn}^{(l)} p_m q_n \tag{24}$$

where

$$p_m = \frac{2aK_a C_m}{\epsilon_m}\psi_m\left(\frac{\epsilon_m x_0}{a}, \frac{\epsilon_n a_0}{a}\right)$$
$$q_n = \frac{2bK_b D_n}{\epsilon_n}\psi_n\left(\frac{\epsilon_n y_0}{b}, \frac{\epsilon_n b_0}{b}\right)$$

and

$$\psi_k(z, s) = [\cosh(z) - \alpha_k \sinh(z)]\sinh(s)$$
$$- [\cos(z) - \alpha_k \sin(z)]\sin(s)$$

with C_m and D_n given by Eq. (6). The expression Eq. (24) is valid when the eigenfunctions are normalized according to Eq. (10). The series in Eq. (24) will, of course, be truncated to a range compatible with the system in Eq. (9). Typical programming routines for finding the eigenvalues λ_l and eigenvectors $A_{mn}^{(l)}$ return the eigenvectors normalized according to Eq. (10); see Ref. 18.

E. Expression for Strain

The strain at a point in the deformed plate can be determined directly from the deformations by[12]

$$\epsilon_{xx} = -\frac{1}{2}h\frac{\partial^2 w}{\partial x^2} \tag{25}$$

and

$$\epsilon_{yy} = -\frac{1}{2}h\frac{\partial^2 w}{\partial y^2} \tag{26}$$

$$\gamma_{xy} = -h\frac{\partial^2 w}{\partial x \partial y} \tag{27}$$

where h is the plate thickness. Note that strain transducers provide a signal that is proportional to the strain averaged over the sensor gauge length. The average normal strains are given by

$$\bar{\epsilon}_{xx} = -\frac{1}{2}h\int_{x_1}^{x_2}\frac{\partial^2 w}{\partial x^2}(x, y)\,dx = -\frac{1}{2}h\left[\frac{\partial w}{\partial x}(x, y_1)\right]_{x_1}^{x_2} \tag{28}$$

$$\bar{\epsilon}_{yy} = -\frac{1}{2}h\int_{y_1}^{y_2}\frac{\partial^2 w}{\partial y^2}(x, y)\,dy = -\frac{1}{2}h\left[\frac{\partial w}{\partial y}(x_1, y)\right]_{y_1}^{y_2} \tag{29}$$

where (x_2, y_1) and (x_1, y_2) are the sensor end points and $\bar{\epsilon}_{xx}$ and $\bar{\epsilon}_{yy}$ are the average strains. The expression for $\partial w/\partial y$ and $\partial w/\partial x$ are

available from Eq. (18) by ordinary differentiation and, in fact, the expressions for local average normal strains at a given sensor are

$$\bar{\epsilon}_{xx} = -\frac{1}{2}h\sum_{l=1}^{\infty}\frac{b_l}{\rho h}\boldsymbol{L}^{-1}\left(\frac{P_0(s)}{s^2+\tilde{a}s+\tilde{b}_l}\right)(t)\left[\frac{\partial w_l}{\partial x}(x, y_1)\right]_{x_1}^{x_2} \quad (30)$$

and

$$\bar{\epsilon}_{yy} = -\frac{1}{2}h\sum_{l=1}^{\infty}\frac{b_l}{\rho h}\boldsymbol{L}^{-1}\left(\frac{P_0(s)}{s^2+\tilde{a}s+\tilde{b}_l}\right)(t)\left[\frac{\partial w_l(x_1, y)}{\partial y}\right]_{y_1}^{y_2} \quad (31)$$

where

$$\frac{\partial w_l}{\partial x} = \sum_{m=1}^{\infty}\sum_{n=1}^{\infty}A_{mn}^{(l)}X_m'(x)Y_n(y) \quad (32)$$

and

$$\frac{\partial w_l}{\partial y} = \sum_{m=1}^{\infty}\sum_{n=1}^{\infty}A_{mn}^{(l)}X_m'(x)Y_n(y) \quad (33)$$

The ordinary derivatives $X_m'(x)$ and $Y_n'(y)$ can be found in closed form from Eq. (3). As an example, the formulation for the average strains already given can be used to predict the average strain locations of a 0.66×0.41 m, 1.57-mm-thick rectangular aluminum plate subjected to transverse impact. A schematic of the plate is provided in Fig. 1, which also shows the locations of four sensors oriented in the y direction and the location of the impact event. The pertinent plate material properties are $\rho = 2752.3$ kg/m^3, $E = 70$ GPa, and $\upsilon = 0.30$. Figure 2 shows the strain responses of the four sensors

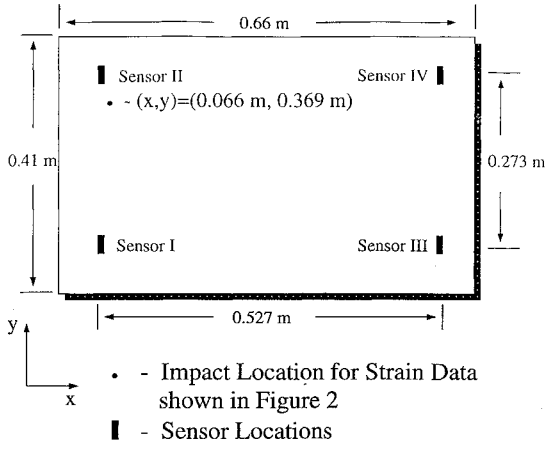

Fig. 1 Aluminum plate test specimen, 1/16 in. thick; sensor and sample impact locations shown.

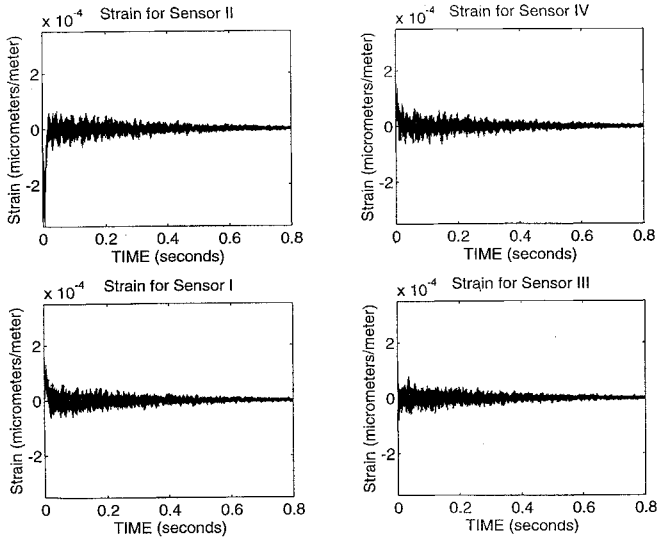

Fig. 2 Strain history at each sensor location for the first 0.8 s after impacting the aluminum plate at the coordinates shown in Fig. 1.

for the impact shown in Fig. 1. Notice that they all show appropriate initial impulse followed by damped vibrational behavior.

III. Impact Location Technique

Examination of the plate dynamics model embodied in Eqs. (30) and (31) showed that the deformation in the plate at the sensor location is governed by the sensor location (encoded in w_l) and the impact location (encoded in b_l). Note that Eqs. (30) and (31) can not be directly inverted to find the impact location because b_l results from nonlinear functions; however, it is possible to train a neural network to invert the system provided appropriate input–output relationships are identified. The idea of providing the entire time-domain response as variables was quickly discarded as this would require as many inputs as there are time steps. Instead, it was realized that the plate response could be compressed into a discrete set of modal descriptors derivable from the frequency response of the plate. Examples of these descriptors are the frequencies and amplitudes, which could be used in series form to reconstruct the entire time-domain response if desired. As a result, various characteristic descriptors of the frequency response of the impacted plate will be used to locate impact events. Note that time-of-flight data could be easily used as input data.[3] The present approach is adopted because it is believed that impact energy can ultimately be determined using modal data as inputs. Time-of-flight data do not provide this option.

The analysis of the series solution Eq. (18) was discussed in the Laplace and time domains; however, as the argument presented earlier points out, it is convenient to collect data in the form of the Fourier transform of local average strain. This is precisely the form of data associated with a sensing section of optical fiber whose signal is submitted to a fast Fourier transform. This scenario of local average strain will be adopted for the remainder of this paper.

A. Fourier Transform of Average Strain

Since it is the Fourier transforms of Eqs. (30) and (31) that serve as data, one must transform these equations, or specifically the term $\boldsymbol{L}^{-1}[P_0(s)/(s^2+\tilde{a}s+\tilde{b}_l](t)$. Fortunately, advantage can be taken of the fact that this expression is already a (Laplace) transform.

Let $\hat{w}(x, y, \omega)$ be the Fourier transform of $u(x, y, t)$,

$$\hat{w}(x, y, w) = \boldsymbol{F}[w(x, y, t)](\omega) = \int_{-\infty}^{\infty} w(x, y, t)e^{j\omega t}\,dt \quad (34)$$

and let

$$F_l(t) = \boldsymbol{L}^{-1}\left[\frac{P_0(s)}{s^2+\tilde{a}s+\tilde{b}_l}\right](t) \quad (35)$$

so that

$$\hat{w}(x, y, \omega) = \sum_{l=1}^{\infty}\frac{b_l}{\rho h}\boldsymbol{F}[F_l(t)](\omega)w_l(x, y) \quad (36)$$

Since $F_l(t) = 0$ for $t < 0$, by definition of the Laplace transform,

$$\boldsymbol{F}[F_l(t)](\omega) = \int_0^{\infty} F_l(t)e^{j\omega t}\,dt = L[F_l(t)](-j\omega) \quad (37)$$

i.e., the Fourier transform is the complex Laplace transform. Then by Eq. (35)

$$\boldsymbol{F}[F_l(t)](\omega) = \left[\frac{P_0(s)}{s^2+\tilde{a}s+\tilde{b}_l}\right]_{s=-j\omega}$$

$$= \frac{P_l(-j\omega)}{-\omega^2 - (cj\omega/\rho h) + (D\tau_l/\rho h)} \quad (38)$$

where $P_0(s)$ is given in Eq. (20). Performing the algebra in Eq. (38) one finds that

$$\boldsymbol{F}[F_l(t)](\omega) = R_l(\omega) + jI_l(\omega) \quad (39)$$

where the real and imaginary parts $R_l(\omega)$ and $I_l(\omega)$ are (complicated) expressions given in the Appendix; see Eq. (A5). Making

contact with Eqs. (30) and (31), the Fourier transform of integrated strain in the x and y directions is thus given by the quantities

$$\boldsymbol{F}(\bar{\epsilon}_{xx})(\omega) = -\frac{h}{2}\sum_{l=1}^{\infty}\frac{b_l}{\rho h}[R_l(\omega) + jI_l(\omega)] \times \left[\frac{\partial w_l}{\partial x}(x_2, y_1) - \frac{\partial w_l}{\partial x}(x_1, y_1)\right] \tag{40}$$

$$\boldsymbol{F}(\bar{\epsilon}_{yy})(\omega) = -\frac{h}{2}\sum_{l=1}^{\infty}\frac{b_l}{\rho h}[R_l(\omega) + jI_l(\omega)] \times \left[\frac{\partial w_l}{\partial y}(x_1, y_2) - \frac{\partial w_l}{\partial y}(x_1, y_1)\right] \tag{41}$$

where it is assumed that the sensor occupies the linear segment from (x_1, y_1) to (x_1, y_2). The amplitude, or real and imaginary parts, of $\boldsymbol{F}(\bar{\epsilon}_{xx})$ and $\boldsymbol{F}(\bar{\epsilon}_{yy})$ follow easily from Eqs. (40) and (41). It should be mentioned that the expressions for $R_l(\omega)$ and $I_l(\omega)$ consist of closed-form built-in functional evaluations and thus permit efficient numerical computation.

B. Neural Network Training

An artificial neural network operates on the basis of a fixed number of input and output processing elements, or "neurons," connected by hidden layers of other neurons. In the case at hand, an integer N will be selected to represent the number of natural frequencies $\lambda_1, \lambda_2, \ldots, \lambda_N$ to be used in the analytical model. It will be assumed that four sensors are mounted on the plate so that strain information, in the form of Eqs. (40) and (41) or otherwise, will be available at four pairs of points (x, y), and at any frequency ω, when an impact occurs at an arbitrary point (x_0, y_0). For a given impact at (x_0, y_0) one could select, for example, the modulus of Eq. (40) at each of the first N frequencies $\omega_l = \tilde{B}_l$, $1 \leq l \leq N$, and at each sensor location for a total of $4N$ inputs. The outputs will be the coordinates x_0 and y_0 of the impact point. If, for instance, the first 16 harmonics are used and there are 100 strike points (x_0, y_0), then the input layer will contain 64 elements, the output layer will contain 2 elements, and thus the training file will run to 6600 lines; each of 100 training episodes will evaluate 66 processing elements. The number of hidden layers, and neurons in each, can be determined by experience. In practice it is usually not necessary to use more than one or two hidden layers.

A neural network learns by repeated iterations through the training file. In most neural network scenarios, connecting weights between neurons are adjusted after each training cycle. However, in cumulative back propagation neural networks, weights are adjusted after several training cycles called epochs. For problems of the type described here, the number of iterations required to reduce the rms error to a few percent typically runs into several tens of thousands, depending on the network architecture and software type. On a desktop computer with a 486 or better coprocesser, it would not normally require more than about 5–15 min to run through 50,000 iterations.

Finally, it is worth mentioning that an additional important motivation for using neural networks for signal processing lies in the uncertainty of amplitude constants such as K_0, K_a, and K_b in Eqs. (19) and (23). On the one hand, it would be difficult to know precise values to assign these and other physical constants associated with the plate; on the other hand, their values do not affect the training and performance of the network. Indeed, the network trains on the basis of relationships between input and output, the specific dynamics of which will not be germane, and performs on the same basis. Specific values of constants affect only the scaling of relationships and will, thus, not affect training, as long as the scaling is uniform. This makes physical sense and is analogous to the fact that a working physical detection system would not depend on, for example, a particular scale signal amplitude but rather on the relative values corresponding to separate events. For this reason amplitude constants in the analytical model may be set at convenient, arbitrary levels.

C. Training and Testing Results

The test article used to design and test neural network-based impact location methodologies is the clamped rectangular aluminum plate shown in Fig. 1. The sensor locations in Fig. 1 were chosen after viewing the first 16 mode shapes. Care was taken so that the sensor did not fall on any nodal lines so that the information content of strain signals could be maximized.[1] The Neural Works Explorer software package, which provides many neural network paradigms, is used to implement the impact detection approaches. After trials with different paradigms, it was discovered that the error back-propagation algorithm provided the fastest convergence and lowest error for damage location detection. The impact location techniques thus far explored include using magnitudes of frequency response data evaluated at the plate modes, the real and imaginary parts of frequency response data evaluated at the plate modes, and the real and imaginary parts of the fast Fourier transform (FFT) of strain integrated over a preset frequency range. In each case, parametric studies were performed to determine the optimum number of plate modes and impacts needed for training nonetheless still providing accurate impact location predictions. This information is important from an experimental expense point of view. Note that for brevity, only detailed results for the number of impacts used in training is provided.

For the magnitude data, a set of input processing elements (nodes) equal to the number of plate modes multiplied by 4 (representing the number of sensors) were used. A hidden layer containing one-half the number of input nodes was used. The output layer contains only two nodes, to determine the damage location coordinates. For the paradigm that uses the real and imaginary parts of the frequency response, a set of input nodes equal to the number of plate modes multiplied by 2 (real and imaginary parts) multiplied by 4 (representing the number of sensors) was used. Again, the hidden layer numbered one-half of the input layer, and the output layer contained only two nodes. For the paradigm that uses the integrated Fourier transform of strain data, two inputs for each of the four sensors (real part of Fourier transform integrated over frequency and imaginary part of Fourier transform integrated over frequency) were used. For this paradigm, two training techniques were attempted. These methods used one hidden layer and two hidden layers, respectively. The networks using one hidden layer contained 16 nodes, and the two hidden layer networks used 16 nodes in the first hidden layer and 8 nodes in the second hidden layer. In almost every case, the two hidden layer networks outperformed the one hidden layer networks, with a lower overall rms error. In each case the output layer contained two nodes for impact location detection.

Training the neural networks was accomplished using two different parametric study techniques. In the first technique, the training sets were equal grids of impacts in the x and y directions (i.e., 9×9, 8×8, etc.). These impacts were equally spaced on the plate (e.g., for the 9×9 grid, $\Delta x = 0.066$ m, $\Delta y = 0.041$ m) to provide maximum coverage of possible outcomes. The second technique uses the physical dimensions of the plate as a guideline for the number of training impacts. Since the width of the plate is approximately 150% of its height, impacts were generated in a 3:2 ratio (width:height). The training sets varied from 6 impacts (3:2) to 70 impacts (10:7). The training set must be sufficiently large for the network to learn the patterns it is taught (generalize). If the training set is not large enough, the network will never converge to a global error minimum or the global error minimum will be too high for practical use. If the training set is too large, saturation will occur, and the network will not converge to a global error minimum.

The test data set used to evaluate the impact location detection approaches contains 100 randomly generated impact locations. The random nature of the testing ensures an accurate method of checking the ability of the networks to generalize. The following expression for rms error criterion is used to provide a quantitative metric of the three proposed impact location approaches:

$$E_{\text{rms}} = \frac{1}{n}\sqrt{\sum_{i=1}^{n}\left[(x - x_i)^2 + (y - y_i)^2\right]}$$

where n is the number of test impacts, x and y are the exact impact coordinates used in the analytical model, and x_i and y_i, are the neu-

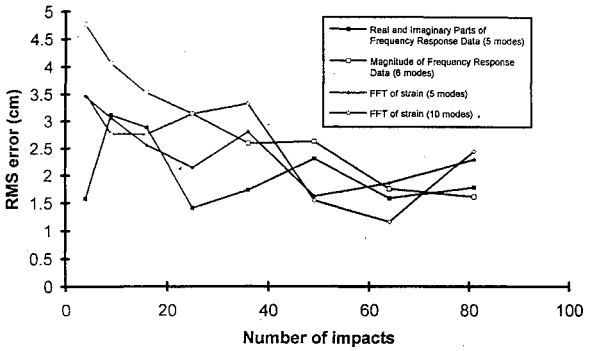

Fig. 3a rms error using training grids with an equal number of impacts in the x and y directions, i.e., 9×9, 8×8, etc.

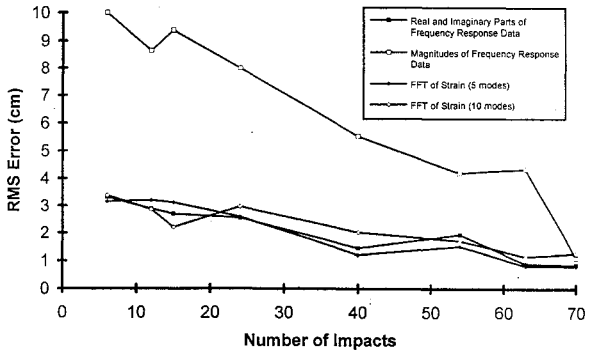

Fig. 3b rms error using nonuniform training grids.

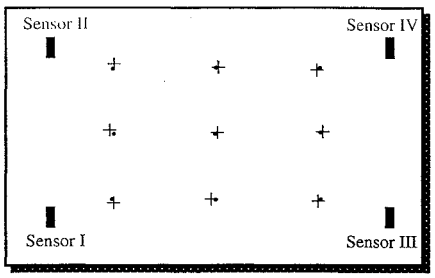

Fig. 4 Sample plate showing coordinates of simulated impacts and their corresponding neural network solutions; the input data used to train the network were the FFT of strain data using the first 10 harmonic natural frequencies: •, actual coordinates of impact; +, neural network solution; ▮, sensor placement.

ral network solutions for the impact coordinates. Figures 3a and 3b show the computed rms error for each impact location paradigm as a function of the number of impact events used during training. Figure 3a corresponds to using $n \times n$ grids for training impacts, whereas Fig. 3b corresponds to using nonuniform training grids. The horizontal axis is chosen to be the number of impacts required to train the network in order to determine the minimum required training set. This is important because experimental training is a time consuming process. These figures show that in each case the magnitude of the frequency response evaluated at the modal frequencies generally performs the worst (this is particularly evident in Fig. 3b). The remaining approaches exhibit roughly equal performance. One important finding of these figures is that the training pattern that conforms to the plate geometry reduces the error of impact location prediction by 20–30%. The final important finding of the data in Fig. 3 is that the integrated FFT data performs as well, or better than, the other techniques that were evaluated. This is important because the integrated FFT approach requires only two inputs per sensor, thereby reducing the complexity of the neural network paradigm and the required sensor data processing and formatting. Note that the number of sensors has not changed for each case, just the way in which the sensor data is utilized. Figure 4 shows a sample plate with locations of actual impact and those predicted by the neural network using the real and imaginary parts of the integrated FFT of the strain data. The integration range included the first 10 modes of the plate

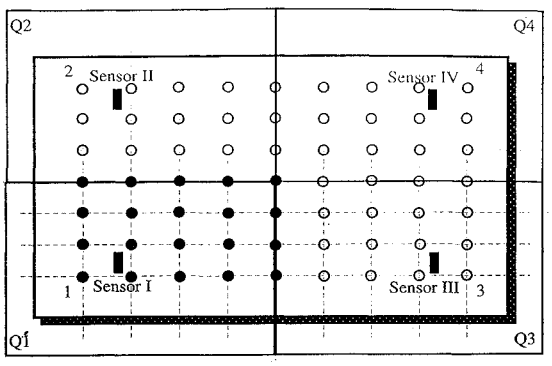

Fig. 5 Sample plate showing the actual and extrapolated impact locations created by taking advantage of the plate's symmetry and performing only 20 actual impacts for a 63 impact training grid: o, extrapolated impact locations; •, actual impact locations.

response. The average rms error of 8 mm per impact location results because the neural network paradigm provides an approximation to the physical system. When viewing Fig. 4 recall that the data used for training the neural network are symmetric with respect to the plate's centerlines, however, the testing data set is not. Each neural network is tested on a set of 100 impacts using random coordinates, so the 9 shown in Fig. 4 represents only a small subset of the test impacts.

Since the test specimen is symmetric, the possibility does exist of using impact data from only one-quarter of the plate. As a test of this idea, a neural network that uses data from 63 impact locations will be retrained using data from the 20 true impact locations, shown in Fig. 5. These data are then mirrored-extrapolated to the remaining 43 points on the plate. The neural network that used 63 actual impact locations for location detection had an rms error of 0.822 radial cm. The neural network that used 20 actual and 43 extrapolated impact locations for location detection had an rms error of 1.2045 radial cm. This shows that the neural networks can be trained to determine impact location by extrapolating data for the other three-quarters of the plate at the expense of slightly greater error.

One of the motivations for investigating neural network-based impact location was that this approach offers the possibility of determining some metric of impact energy. This can be accomplished by training the second neural network paradigm with the same impact locations as the first, but with varying impact magnitude levels. If the neural network responsible for impact location was trained using N impact locations, the magnitude detection could be done by choosing n impact magnitude level increments and training the magnitude of impact neural network on $n \times N$ impacts. For every one impact location that the location neural network trains on, the magnitude of impact neural network trains on n impacts in the same location, with each having different impact magnitudes. The major problem with this method is that training impacts could easily exceed 1000, making this process extremely time intensive.

To verify this concept, a total of eight neural networks were trained as a preliminary test. Each neural network had 10 input processing elements, 7 processing elements in the first hidden layer, 3 processing elements in the second hidden layer, and 1 output processing element. The input data were the integrated real and imaginary parts of the FFT of strain data, evaluated over the first five modes, and the output was the contact pressure level which corresponds to the maximum amplitude of the force input to the analytical model for impact transverse events. Of these eight neural networks, four used a 40 impact training grid and four used a 63 impact training grid. For each training grid configuration, neural networks used 5, 10, 15, and 20 impact magnitude increments equally spaced between 5 and 50 MPa.

To quantitatively estimate the performance of these networks, an rms error was defined as follows:

$$E_{\text{rms}}(\%) = \frac{1}{n}\sum \left| \frac{\text{pressure(actual)} - \text{pressure(computed)}}{\text{pressure(actual)}} \right| \times 100$$

where pressure (actual) is the contact pressure loading input to the

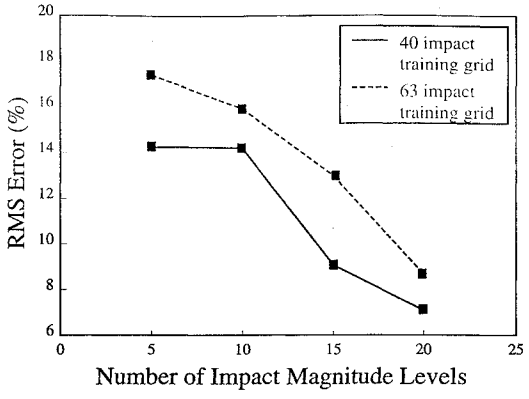

Fig. 6 rms error for 40 and 63 impact training grids, using 5, 10, 15, and 20 impact magnitude increments spaced equally between 5 and 50 MPa.

impact model and pressure (computed) is the contact pressure calculated by the neural network.

Figure 6 shows the percent rms between the actual and computed pressures on the vertical axis, which is plotted against the number of impact magnitude levels on the horizontal axis. In each case, the testing file contains 100 impacts with random location and random impact magnitude varying from 5 to 50 MPa. The results in Fig. 6 indicate the general trend that the 40 impact training grid has less error than the 63 impact training grid, regardless of the number of impact magnitude increments. The minimum error for all neural networks tried is the network using a 40 impact training grid and 20 impact magnitude increments. The rms error for this case was 7.08%. This is promising, but performing 800 experimental impacts would be too time consuming for practical use. Perhaps this method could be used if the number of impacts can be reduced to a reasonable amount. Another possible method of impact location and impact magnitude detection involves using a neural network that simultaneously estimates both of these output parameters, but this idea is yet to be tested.

IV. Discussion

This paper has detailed a mathematical model of the time-dependent response of a fully clamped, isotropic, homogeneous, linear elastic rectangular plate to transverse impact events. The details of the time and space dependence of the impact force are relaxed slightly to obtain a closed-form solution. This solution is then used to generate simulated sensor response data that are used in evaluating potential neural network-based impact location methodologies. The most successful impact location methodology uses FFT of the strain integrated over frequency. This impact location methodology is now a prime candidate for the experimental implementation we are currently undertaking. There are many implementation issues regarding the purpose of impact detection approach that are best understood through experiment. These include the influences of 1) boundary conditions that evolve over time, 2) sensor type and gauge length, and 3) noise and experimental error. Clearly the boundary conditions in any structural system will evolve with time and will result in a modified modal response, which in turn would change the overall predictive capability of a neural network trained based on virgin conditions. Similar comments could be made for nonideal boundary conditions as well. This may then imply that any neural network-based damage detection methodology may require an "continuing education" in reference to the undamaged modal response of the structure. The degree to which systematic noise will inhibit the neural network training can be addressed on a heuristic level. Clearly, the quality of the data used in the training set will govern the overall accuracy of the impact detection methodology. However, the noise levels present in any measurement can be modified through appropriate choice of filters or sensor types. The degree of requisite postprocessing will depend on everything from the quality of the instrumentation to the aptitude of the experimenters. As an example, initial tests using resistance strain gauges with no postprocessing have proven capable of locating impacts within an rms error of 8 mm.

Appendix: Expanded Solutions

A. Characteristic Matrix

With $X_n(x)$ and $Y_n(y)$ defined by Eq. (3), let[17]

$$H_{km} = a\int_0^0 X_i'(x)X_m'(x)\,dx$$

$$K_{km} = b\int_0^b Y_k'(y)Y_n'(y)\,dy$$

and then

$$C_{mn}^{ik} = \begin{cases} \dfrac{a}{b}\epsilon_i^4 + \dfrac{a^3}{b^3}\epsilon_k^4 + \dfrac{2a}{b}H_{im}K_{kn}, & (m,n) = (i,k) \\ \dfrac{2a}{b}H_{im}K_{kn}, & (m,n) \neq (i,k) \end{cases} \tag{A1}$$

In practice Eq. (9) will be truncated to the form

$$\sum_{m=1}^{m_0}\sum_{n=1}^{n_0}\left(C_{mn}^{ik} - \lambda_l\delta_{mn}^{ik}\right)A_{mn}^{(l)} = 0 \tag{A2}$$

with the understanding that $\lambda_l = \lambda_l^{m_0,n_0}$ and that $\lambda_l^{m_0,m_0}$ approaches the correct eigenvalue as $m_0, n_0, \to \infty$. This convergence is in fact quite rapid,[17] and it is usually not necessary to use more than about a 4×4 version of Eq. (A2). In the case that $m_0 = n_0 = 2$, Eq. (A2) becomes

$$\begin{aligned} \left(C_{11}^{11} - \lambda\right)A_{11} + C_{12}^{11}A_{12} + C_{21}^{11}A_{21} + C_{22}^{11}A_{22} &= 0 \\ C_{11}^{12}A_{11} + \left(C_{12}^{12} - \lambda\right)A_{12} + C_{21}^{12}A_{21} + C_{22}^{12}A_{22} &= 0 \\ C_{11}^{21}A_{11} + C_{12}^{21}A_{12}\left(C_{21}^{21} - \lambda\right)A_{21} + C_{22}^{22}A_{22} &= 0 \\ C_{11}^{22}A_{11} + C_{12}^{22}A_{12} + C_{21}^{22}A_{21} + \left(C_{22}^{22} - \lambda\right)A_{22} &= 0 \end{aligned} \tag{A3}$$

Typical software packages include the option of normalizing the solution of Eq. (A3)[18] to the form of Eq. (10).

B. Time Dependence

In Eq. (21) the full solution is

$$\begin{aligned} &\frac{2K_0H(t-t_0)e^{-\tilde{a}(t-t_0)/2}}{\left(M^2+\tilde{a}M+\tilde{b}_l\right)\left(M^2-\tilde{a}M+\tilde{b}_l\right)}\left[\frac{\left(M^2+b_l\right)\sin[\tilde{B}_l(t-t_0)]}{\tilde{B}_l}\right. \\ &\left. -\tilde{a}M\cos[\tilde{B}_l(t-t_0)]\right] + \frac{K_0e^{M(t-t_0)}}{M^2+\tilde{a}M+\tilde{b}_l}[1-H(t-t_0)] \\ &+\frac{K_0e^{-M(t-t_0)}}{M^2-\tilde{a}M+\tilde{b}_l}H(t-t_0) - \frac{K_0e^{-Mt_0}e^{-\tilde{a}t/2}}{M^2+\tilde{a}M+\tilde{b}_l} \\ &\times\left[\frac{(M+\tilde{a}/2)\sin(\tilde{B}_lt)}{\tilde{B}_l} + \cos(\tilde{B}_lt)\right] \end{aligned} \tag{A4}$$

so that $R(t, t_0, l)$ represents the last four terms in Eq. (A4). Note that the growing exponential $e^{M(t-t_0)}$ is annihilated by $1 - H(t-t_0) = 0$ for $t > t_0$. All of the terms in Eq. (A4) are quickly evaluated by computer.

C. Fourier Transform of Strain

It can be calculated that the real and imaginary parts $R_l(\omega)$ and $I_l(\omega)$ in Eq. (39) are given by

$$\begin{aligned} R_l(\omega) = &\frac{M\left[\omega^2 - (D\tau_l/\rho h)\right]\left[e^{-Mt_0} - 2\cos(\omega t_0)\right]}{(M^2+\omega^2)\left\{\left[\omega^2 - (D\tau_l/\rho h)\right]^2 + (c^2\omega^2/\rho^2h^2)\right\}} \\ &- \frac{(c\omega/\rho h)\left[\omega e^{Mt_0} + 2M\sin(\omega t_0)\right]}{(M^2+\omega^2)\left\{\left[\omega^2 - (D\tau_l/\rho h)\right]^2 + (c^2\omega^2/\rho^2h^2)\right\}} \end{aligned} \tag{A5a}$$

and

$$I_l(\omega) = -\frac{(c\omega M/\rho h)\left[e^{-Mt_0} - 2\cos(\omega t_0)\right]}{(M^2+\omega^2)\left\{\left[\omega^2 - (D\tau_l/\rho h)\right]^2 + (c^2\omega^2/\rho^2 h^2)\right\}}$$

$$-\frac{\left[\omega^2 - (D\tau_l/\rho h)\right]\left(\omega e^{Mt_0} + 2M\sin(\omega t_0)\right)}{(M^2+\omega^2)\left\{\left[\omega^2 - (D\tau_l/\rho h)\right]^2 + (c^2\omega^2/\rho^2 h^2)\right\}} \quad \text{(A5b)}$$

Once again, the terms in Eq. (A5) are uncomplicated for a high-speed computer.

Acknowledgments

Partial support of the Office of Naval Research and Army Research Office Contract DAAL-03-72-G-0121 is gratefully acknowledged.

References

[1]Sirkis, J. S., Shaw, K., Berkoff, T. A., Kersey, A. D., Friebele, E. J., and Jones, R. T., "Development of an Impact Detection Technique Using Optical Fiber Sensors and Neural Networks," *Smart Structures and Materials 1994: Smart Sensing, Processing, and Instrumentation*, Society of Photo-Optical Instrumentation Engineers, Orlando, FL, Vol. 2191, 1994, pp. 158–165.

[2]Kudva, J. N., Munir, N., and Tan, P. W., "Damage Detection in Smart Structures Using Neural Networks and Finite-Element Analysis," *Smart Materials and Structures*, Vol. 1, No. 2, 1992, pp. 108–112.

[3]Gunther, M. F., Wang, A., Fogg, R. P., Starr, S. E., Murphy, K. A., and Claus, R. O., "Fiber Optic Impact Detection and Location System Embedded in a Composite Material," *Fiber Optic Smart Structures and Skins V*, Society of Photo-Optical Instrumentation Engineers, Boston, MA, Vol. 1798, 1992, pp. 262–269.

[4]Elkordy, M. F., Chang, K. C., and Lee, G. C., "Neural Networks Trained by Analytically Simulated Damage States," *Journal of Computing in Civil Engineering*, Vol. 7, No. 2, 1993, pp. 130–145.

[5]Regalbrugge, M. E., and Calalo, R., "Probabilistic Neural Network Approaches for Autonomous Identification of Structural Dynamics," *Journal of Intelligent Material Systems and Structures*, Vol. 3, No. 4, 1992, pp. 572–584.

[6]Vadali, S. R., Singh, T., Kurdila, A. J., and Junkins, J. L., "Neural Network Based Control of Large Structures," *Smart Structures and Materials 1993: Smart Structures and Intelligent Systems*, Society of Photo-Optical Instrumentation Engineers, Albuquerque, NM, Vol. 1917, Pt. 2, 1993, pp. 895–906.

[7]Spillman, W. B., Houston, D. R., Fuhr, P. L., and Lord, J. R., "Neural Network Damage Detection in a Bridge Element," *Smart Structures and Materials 1993: Smart Sensing, Processing, and Instrumentation*, Society of Photo-Optical Instrumentation Engineers, Albuquerque, NM, Vol. 1918, 1993, pp. 288–299.

[8]Bryant, M. D., Fernandez, D., Wang, N., Murty, V. V., Vadlamani, V., and West, T. S., "Active Vibration and Control in Structures Using Magnetostrictive Terfenol With Feedback and/or Neural Network Controllers," *Journal of Intelligent Material Systems and Structures*, Vol. 4, No. 4, 1993, pp. 484–489.

[9]Sperring, C. W., Chow, D. E., Mulcahy, D. E., Davey, D. E., and Haskard, M. P., "A Neural Network Applied to Sensor Signal Processing: Determination of Copper in Water," *Journal of Intelligent Material Systems and Structures*, Vol. 3, No. 3, 1992, pp. 418–431.

[10]Warburton, A. B., *The Dynamical Behavior of Structures*, Pergamon, Oxford, England, UK, 1976.

[11]Voltera, E., and Zachmanoglou, E. C., *Dynamics of Vibrations*, C. E. Merrill, Columbus, OH, 1965.

[12]Timoshenko, S., and Woinowsky-Kriager, S., *Theory of Plates and Shells*, 2nd ed., McGraw-Hill, New York, 1959.

[13]Yang, J. C. S., "Impact on Plates and Shells," *International Journal of Solids and Structures*, Vol. 7, No. 5, 1971, pp. 445–458.

[14]Ewins, D. J., *Modal Testing: Theory and Practice*, 1st ed., Research Studies, Letchworth, England, UK, 1986.

[15]Schienberg, W. P., Kerr, L. M., and Woo, T. K., "Low Velocity Impact of Transversely Isotropic Beams and Plates," *International Journal of Solids and Structures*, Vol. 23, No. 7, 1987, pp. 871–896.

[16]Wu, X., Ghaboussi, J., and Garret, J. H., "Compendium: Use of Neural Networks in Detection of Structural Damage," *Computers and Structures*, Vol. 42, No. 3, 1992, pp. 649–659.

[17]Young, D., "Vibration of Rectangular Plates by the Ritz Method," *Journal of Applied Mechanics*, Vol. 17, No. 4, 1950, pp. 448–453.

[18]Press, W. H., Flannery, B. P., Tenkolsky, S. A., and Vetterling, W. T., *Numerical Recipes*, 1st ed., Cambridge Univ. Press, Cambridge, England, UK, 1988, pp. 353–396.